This is the author's version (accepted manuscript) of the work that was accepted for publication in the Journal of Aircraft.
The Version of Record is available online at https://doi.org/10.2514/1.C037506

Aircraft simulations using the new CFD Software from ONERA, DLR, and Airbus

Pedro Stefanin Volpiani*, Jean-Baptiste Chapelier†
ONERA, The French Aerospace Lab, 8 Rue des Vertugadins, 92190 Meudon, France

Axel Schwöppe‡, Jens Jägersküpper§
German Aerospace Center (DLR), Lilienthalplatz 7, 38108 Braunschweig, Germany

Steeve Champagneux¶
Airbus Operations S.A.S., 316 route de Bayonne, 31060 Toulouse, France

This paper presents a thorough comparison between RANS simulations performed with the CFD by ONERA, DLR, AIRBUS (CODA) new generation flow solver and reference legacy codes TAU (DLR) and elsA (ONERA) for high-speed cruising NASA Common Research Model (CRM) configurations that were considered in the context of the 5th, 6th and 7th Drag Prediction Workshops (DPW). The solver accuracy is assessed with several meshing strategies, including block-structured, hybrid structured/unstructured and fully unstructured tetrahedral meshes. This solver features both a cell-centered finite-volume (FV) scheme suited to arbitrary meshes as well as a modern high-order Discontinuous Galerkin (DG) scheme. We show that for all cases considered, the FV component recovers an equivalent accuracy compared to elsA (cell-centered FV) on block-structured meshes and TAU (node-centered FV) on hybrid and unstructured meshes. The high-order DG scheme (third order accurate) is found to enhance significantly the drag prediction on coarse meshes compared to legacy FV methods, both for structured and unstructured meshes.

I. Introduction

Over the past decades, aerodynamic characterization and design activities have benefited from progress in the field of CFD (Computational Fluid Dynamics) simulations and their widespread implementation combined with traditional ground and flight testing. Today, CFD techniques have become mature and indispensable, contributing both to the reduction of overall aircraft design turnaround time and to an ever more exhaustive exploration of aircraft concepts and configurations at a controlled cost. This momentum will certainly continue in the future, supported by technical advances to come, see [1]. Since the introduction of CFD methods in the 1980s, Airbus has continuously implemented

---

*Research scientist, ONERA, Department of Aerodynamics, Aeroelasticity and Acoustics, Civil aircraft unit.

†Research scientist, ONERA, Department of Aerodynamics, Aeroelasticity and Acoustics, Numerical methods team.

‡Team leader, Institute of Aerodynamics and Flow Technology, CASE department, CODA core team

§Scientific researcher, Institute of Aerodynamics and Flow Technolog, CASE department, CODA core team.

¶Engineer, Flight Physics Capabilities Development.

a series of flow solver codes developed by DLR and ONERA to support the design of all its aircraft families. Today, the rationalization and modernization of the portfolio of legacy simulation software currently in operation associated with an ever more demanding verification and validation (V&V) approach has become an absolute necessity, certainly with an obvious concern for simplification, but also to benefit from synergies in activities such as upstream research, software development, industrialization and operational use as well as in technical skills. In this spirit, the CFD by ONERA, DLR, AIRBUS (CODA) new generation flow solver has been developed as part of a collaboration between the French Aerospace Lab ONERA, the German Aerospace Center (DLR), Airbus, and their European research partners with the ambition to cover all their respective needs. This software is jointly owned by ONERA, DLR and Airbus.

The Drag Prediction Workshop (DPW) database provides an impartial environment for evaluating the effectiveness of existing computer codes and modeling techniques using Navier-Stokes solvers. The NASA Common Research Model (CRM) has been used in many workshops and is a well-documented test-case to assess the accuracy of numerical methods in the prediction of aircraft forces and moments. The CRM arrangement was initially designed by Boeing and fabricated and tested by NASA [2] and is representative of existing airliners configurations. Experiments of the CRM have been performed in several research facilities [3–5]. Data from various wind tunnels indicate that the wing pressure distribution is well retrieved between teams. However, force and moment data exhibit some discrepancies. To represent free air flight condition, wind tunnel corrections must be applied to the “raw” measured data. These adjustments help to account for wind tunnel walls, mounting system, nonuniform flow, Mach blockage, lift interference, and so on, but they can affect force and moment data [6]. The DPW uses common public-domain subject geometries, simple enough to permit high-fidelity CFD computations. The availability of the simple CRM geometry and meshes allowed several research groups to participate and contribute to the forum [7–13]. Analyses revealed that when the wind-tunnel model was tested, the wings twisted more than expected and did not match the nose-down twist of the original DPW-5 wing geometry used for the computational studies [14–17]. The inconsistencies of the wing shape could influence considerably the aerodynamic flow field and alter in particular the drag and pitching moment predictions. In the following workshop, DPW-6, the wing geometry was corrected and a better agreement between CFD and experiments was reported [6]. In the latest workshop, DPW-7, also the CRM model was used, to focus on the effect of shock-induced separation on lift and pitching moment.

In this article, we propose to use the NASA Common Research Model wing-body geometry (without tail) to evaluate CODA. The paper is organized as follows: in II, the CRM geometry, the flow conditions and the meshes employed in the computations are outlined. In III, the solvers elsA, TAU and CODA used in this study are presented and their numerical methods are briefly explained. In IV, we briefly describe the near- and far-field drag (FFD) breakdown using the FFDπ software. In V, iso-lift comparisons are performed. We validate CODA and discuss the best practices concerning the input parameters used in the numerical scheme. A comparative grid convergence study on fully-hexahedral structured and mixed unstructured meshes is presented and a code-to-code comparison is performed. In VI, analyses are performed

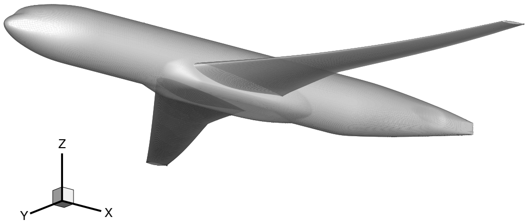

Fig. 1 CRM wing-body configuration, lower-front view.

at fixed angle of attack. Grid convergence studies are presented for structured and unstructured meshes. We also investigate the influence of high-order (HO) finite-element schemes in the computed solution. Finally, a summary is presented in the last section.

II. NASA Common Research Model Geometry and Grids

The NASA Common Research Model (CRM) consists of a contemporary supercritical transonic wing and a fuselage that is representative of a wide-body commercial transport aircraft. It was designed for a cruise Mach number of $M_\infty = 0.85$, Reynolds number based on the mean-aerodynamic chord of $Re = 5 \times 10^6$, and a corresponding design lift coefficient of $C_L = 0.5$. The free-stream reference temperature is set equal to 310K. Experiments have been conducted at the same conditions in the National Transonic Facility transonic wind-tunnel [14]. A sketch of the CRM configuration is shown in Figure 1. The reference geometry is defined by mean-aerodynamic chord $c = 7.00532$ m, reference surface area $S_{\text{ref}} = 383.68956$ m^2 (full model), semispan $b = 29.38145$ m, aspect ratio $AR = 9.0$, and moment center $X_{\text{ref}} = 33.67786$ m, $Y_{\text{ref}} = 0.0$ m, and $Z_{\text{ref}} = 4.51993$ m.

Many grid types are available for download from the DPW website. In this study, we consider three types of grids: (i) full-hexahedral structured, (ii) mixed unstructured, and (iii) full-tetrahedral meshes. First, we conducted simulations using the family of structured multiblock (MB) grids generated by Vassberg [18] and modified by Hue [15] to take into account the wing twist observed in the experiments. These grids can be downloaded from [19]. Five grid-refinement levels were investigated. The number of elements on these grids ranges from 638,976 to 40,894,464 hexahedra. In increasing size order, the members of this family are named: tiny, coarse, medium, fine and extra fine, and labeled L1, L2, L3, L4 and L5, respectively. The medium mesh is representative of current practices for aircraft RANS simulations. These meshes are O-type grids created by extrusion of the surface discretization and they are composed of five structured blocks. This strategy allows a precise control of the grid quality, such as grid spacing, stretching ratio, and grid orthogonality near configuration surfaces. The normal spacing of the first cell next to the wall varies from $Y^+ = 2$ for the tiny grid to $Y^+ = 0.5$ for the extra fine mesh. The mesh extent is greater than 100 mean-aerodynamic chords. The different characteristics of these meshes are presented in Table 1.

We also conduct simulations using families of the original (REV01) DPW-5 multi-block grids converted to hexahedra

Table 1 CRM multiblock structured grids provided by the DPW-5 Committee.

Level	Name	Hexahedra	Nodes	Y^+
L1	Tiny	638,976	660,177	2.00
L2	Coarse	2,156,544	2,204,089	1.33
L3	Medium	5,111,808	5,196,193	1.00
L4	Fine	17,252,352	17,441,905	0.67
L5	Extra-fine	40,894,464	41,231,169	0.50

Table 2 CRM mixed-element, unstructured grids provided by the DPW-5 Committee.

Level	Name	Elements	Nodes
L1	Tiny	2,981,888	660,177
L2	Coarse	10,063,872	2,204,089
L3	Medium	24,068,096	5,196,193
L4	Fine	80,990,208	17,441,905
L5	Extra-fine	192,544,768	41,231,169

(hexahedra and node counts correspond to Table 1) and hybrid unstructured grids, Table 2. For the hybrid grids each hexahedron is divided into tetrahedra or prisms in the boundary layer. These grids can be downloaded from [20]. Five grid-refinement levels were investigated. The naming is the same as for the multi-block grids. The original grids do not take into account the experimental wing twist correction.

Regarding the DPW-6, we considered two mixed unstructured grids discretizing the full geometry of the CRM wing-fuselage configuration (without symmetry plane). The coarse grid has 27.9 M elements and the fine one 53.2 M as reported in Table 3. More information is available in [21]. More akin to the validation of high-order methods, we also consider a CRM case and mesh family originating from the 5th High-Order Workshop (HOW-5 [22]). The geometry and flow conditions for this test case correspond to the third test case of DPW-6 (angle of attack sweep) with a single angle of attack of 2.75 degrees. The HOW-5 website provides a series of 9 meshes for grid convergence studies, with the particularity of being composed of only tetrahedra, even in the near-wall region, see [23]. Those meshes are particularly challenging for the element-based FV and DG numerical methods considered in CODA.

For DPW-7, DLR provided a series of unstructured meshes to the committee that were generated with the SOLAR grid generation software, which is a common practise in combination with the DLR TAU code. These meshes can be downloaded from [24]. Table 4 lists sizes of these official DPW-7 meshes. About three quarters of the elements are tetrahedrons, which discretize the computational domain of the CRM geometry, whereas in the meshing of the boundary

Mesh name	Hexa	Prisms	Pyramids	Tetrahedra	Total elements	Total nodes
UM1	11,950,486	3,003,697	524,240	12,383,848	27,862,271	15,808,438
UM2	11,950,622	3,003,578	524,416	37,755,443	53,234,059	20,011,255

Table 3 Mixed unstructured grids of the DPW-6 CRM wing-fuselage configuration.

Table 4 CRM unstructured Solar grids provided by the DPW-7 Committee.

Level	Name	Elements	Nodes
L1	Tiny	31,589,359	11,698,938
L2	Coarse	64,334,695	25,007,998
L3	Medium	130,749,024	47,064,610
L4	Fine	224,104,611	76,507,952
L5	Extra-fine	367,929,107	118,857,926
L6	Ultra-fine	534,174,466	164,527,472

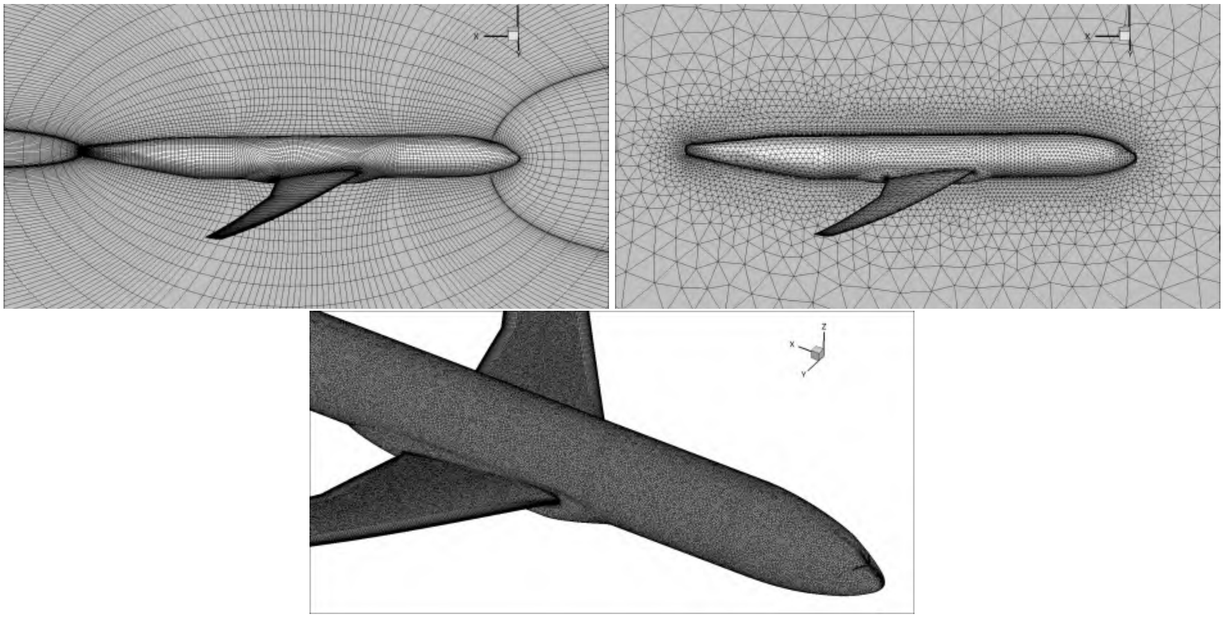

Fig. 2 Example of meshes employed in this study: full-structured (L1-DPW5), full-tetrahedra (L2-HOW5) and mixed unstructured (UM1-DPW6) meshes.

layer, hexahedrons dominate (quad-dominant wall surface mesh). Note that the number of elements for the medium mesh is already larger than the number of nodes in the extra-fine mesh. This remark is important since the number of degrees-of-freedom (DoF) is defined by the number of elements for the cell-centered software CODA and by the number of nodes for node-centered codes such as TAU. When comparing these two codes in Sec. VI.B, we need to account for this difference of the metrics applied by these two codes.

Figure 2 shows some of the meshes employed in this study: full-structured, full-tetrahedra and mixed unstructured meshes.

III. Solvers

A. CODA

This new generation flow solver operates on unstructured meshes in cell-centered fashion and combines established finite-volume (FV) schemes with high-order Discontinuous-Galerkin (DG) methods. It was designed for efficient simulations on highly parallel and heterogeneous High Performance Computing (HPC) architectures, applying modern software design and coding techniques. CODA implements a hybrid distributed/shared memory parallel approach based on MPI and multithread, to benefit the most from modern processor architecture [25]. The linear algebra library Spliss is GPU-compatible in order to optimize the time spent solving linear systems related to implicit time integration or adjoint problems solving [26].

1. Finite-volume discretization

The finite-volume discretization is designed to be second-order accurate. It is important to formulate the discretization with respect to the properties of the underlying cell-centered grid metric, especially for non-smooth and unstructured meshes. For the discretization of convective terms multiple schemes are available. In the present work we focus on Roe's (upwinding) scheme with entropy fix. For the Roe scheme state values left and right at a cell face are gradient-based, piecewise linearly reconstructed. Therefore, the accuracy of the discretization depends essentially on the method to compute element gradients.

Element gradients Element gradients are computed based on the Green-Gauss theorem or on the weighted least-squares method. The latter defines a stencil that contains neighboring elements used to calculate an element gradient. In addition to the usual face-based stencil, that contains those elements which share a common face with the considered element, a so-called extended stencil is available. There, the element neighborhood is defined by all elements that share at least one node (rather than a common face). The extended stencil is discussed in detail in [27], along with further stencil extensions. The weighted least-squares gradient computation uses the extended stencil to overcome robustness issues which can be observed using only the face-based stencil on unstructured meshes. Furthermore, the Green-Gauss gradient approach is extended to overcome accuracy issues on non-smooth meshes following [28]. Green-Gauss gradients reconstruct values needed at face integration-points to approximate the Green-Gauss (GG) integral linearly. Standard Green-Gauss (stdGG) gradients use a linear interpolation between element-averaged values of the neighbouring elements of a face. This interpolation introduces an integration error on non-smooth meshes because the location of the interpolated value differs from the face integration-point. Extended Green-Gauss (extGG) gradients use a weighted least-squares gradient-based, piecewise linear reconstruction taking the extended stencil into account. Reconstruction point and face integration-point are on top of each other. Hence, the extGG gradient approach avoids integration errors introduced by usage of stdGG gradients on both non-smooth, structured and non-smooth, unstructured meshes. Gradient limiters can be applied near strong discontinuities, for instance those from Barth and Jespersen [29] or Venkatakrishnan [30]. The 'spline quintic' limiter is an alternative to Venkatakrishnan's limiter based upon a quintic spline approximation of the limiter function.

Face gradients For the discretization of terms like the diffusive part that require gradients at faces integration-points, multiple "face-gradient augmentation" schemes are available. These allow trading accuracy for robustness to some extend. Gradients at a face are computed as average of the adjacent element gradients. The average of the element gradients is augmented. The augmentation avoids odd-even decoupling, which may lead to loss of robustness, by replacing the projection of the gradient regarding the face by a more compact gradient approximation [31]. The 'edge' augmentation replaces the projection of the element gradient regarding the edge (the straight line between the adjacent element centers) by the slope computed from the element states w.r.t. the length of the edge. The 'edge' augmented face gradient of an element at a face integration point is computed as

$$\nabla\phi_{en} = \nabla\phi_e + \left[\frac{\phi_n - \phi_e}{e_{e,n}} - \nabla\phi_e \mathbf{e}_{e,n}\right]\mathbf{e}_{e,n}, \tag{1}$$

where $\nabla\phi_e$ denotes the element state value gradient of element e, ϕ_e the average state value of element e, ϕ_n the average state value of the adjacent element n, $\mathbf{e}_{e,n}$ the unit vector from the element center $\mathbf{x}_e$ to the adjacent element center $\mathbf{x}_n$, and $e_{e,n}$ the length of the vector from the element center $\mathbf{x}_e$ to the adjacent element center $\mathbf{x}_n$. The 'face' augmentation replaces the projection of the element gradient regarding the face normal by the slope computed from the element states w.r.t. the length of the edge projected on the face normal. The 'face' augmented face gradient of an element at a face integration point is computed as

$$\nabla\phi_{en} = \nabla\phi_e + \left[\frac{\phi_n - \phi_e}{e_{e,n}\mathbf{e}_{e,n}\cdot\mathbf{n}_{e,n}} - \nabla\phi_e\cdot\mathbf{n}_{e,n}\right]\mathbf{n}_{e,n}, \tag{2}$$

where $\mathbf{n}_{e,n}$ denotes the unit normal vector of the face. The 'cell-to-face' augmentation replaces the projection of the element gradient regarding the straight line between the element center and the face integration-point by the slope computed from the element state and face state, which is interpolated linearly between adjacent element states, w.r.t. the length of this vector. The 'cell-to-face' augmented face gradient of an element at a face integration point is computed as

$$\nabla\phi_{en} = \nabla\phi_e + \left[\frac{\phi_f - \phi_e}{e_{e,f}} - \nabla\phi_e\cdot\mathbf{e}_{e,f}\right]\mathbf{e}_{e,f}, \tag{3}$$

where $\mathbf{e}_{e,f}$ denotes the unit vector from the element center $\mathbf{x}_e$ to the face integration-point $\mathbf{x}_f$, $e_{e,f}$ the length of the vector from the element center to the face integration-point, and ϕ_f the state value at the face integration-point, computed as a weighted average of ϕ_e and ϕ_n

$$\phi_f = \alpha_e \phi_e + \alpha_n \phi_n, \tag{4}$$

where the edge weights α_e and $\alpha_n = 1 - \alpha_e$ are the projected weights. A projected edge weight w.r.t. to an element is computed as

$$\alpha_e = \frac{\left|\left(\mathbf{x}_\mathbf{n} - \mathbf{x}_f\right) \cdot \mathbf{e}_{\mathbf{e},\mathbf{n}}\right|}{\left|\left(\mathbf{x}_\mathbf{n} - \mathbf{x}_f\right) \cdot \mathbf{e}_{\mathbf{e},\mathbf{n}}\right| + \left|\left(\mathbf{x}_\mathbf{f} - \mathbf{x}_e\right) \cdot \mathbf{e}_{\mathbf{e},\mathbf{n}}\right|}. \tag{5}$$

For a Cartesian-like mesh with uniform or non-uniform spacing all cell-to-face, face and edge augmentation yield the same discretization. For non-smooth meshes the slope used by the 'face' augmentation 2 to replace the projection of an element gradient may be computed w.r.t. a shortened length of the edge, which can lead to more diffusion compared to the edge augmentation. The additional diffusion can improve robustness of an iteration process but may also have a distinct effect on the numerical solution if the diffusive part of the physical model dominates the character of the computed case. For non-smooth meshes the slope used by the 'cell-to-face' augmentation 3 to replace the projection of an element gradient includes an interpolation error introduced by the linearly interpolated face state. Therefore, the most accurate 'edge' augmentation should be used especially for meshes with strongly non-smooth boundary layer resolution like fully tetrahedral meshes.

2. *Discontinuous-Galerkin discretization*

The Discontinuous-Galerkin discretization is based on a modal approach that relies on the use of a hierarchical and orthogonal polynomial basis for the Galerkin projection. The discretization of the viscous terms is performed using the BR1 [32] or BR2 [33] approaches. For more detail about the DG formulation and examples of applications related to $DG - hp$ adaptation of turbulent flows using CODA, see [34, 35].

3. *Temporal discretization*

Temporal integration is performed by employing an implicit backward-Euler scheme relying on the matrix-free GMRES block-Jacobi method, where the Jacobi method may apply element (i.e. block) local LU or a lines-inversion method as preconditioner.

B. elsA solver

Since one of our objectives is to validate and understand the best settings when performing simulations with CODA, we chose to compare the numerical results with an already established code in the literature. The elsA Navier-Stokes solver uses a cell-centered finite-volume discretization on structured point-matched or overset grids [36]. In this study, time integration is performed using a backward-Euler scheme with implicit LU-SSOR relaxation. Spatial discretization is realized using a second-order central Jameson scheme [37] with artificial viscosity as done in [15]. In this paper, elsA results were obtained using version 4.1.01 (Airbus-Safran-ONERA property).

C. TAU

The DLR TAU code is a Navier-Stokes solver widely established in European aerospace industry as well as academia. It uses a node-centered finite-volume discretization on mixed element grids [38]. In this study, the time integration is performed using a backward-Euler scheme with implicit LU-SGS relaxation [39]. Spatial discretization is realized using a second-order central scheme with matrix dissipation [38] based on the Jameson scheme [37]. The following code-to-code comparisons of CODA with TAU use the TAU version 2021.1.0.

D. Turbulence Modeling

All flow simulations performed in the present study are considered fully turbulent. Whatever the flow solver considered, the one-equation Spalart-Allmaras (SA) formulation is used as the closure for the compressible/ RANS equations to model turbulence effects . More specificaly, elsA simulations are conducted with the variant of the SA model described in [40] while the "negative" formulation described in [41] is used for both TAU and CODA simulations.

IV. Near-Field and Far-Field Drag analysis using FFDπ

In the near-field analysis, the total drag is split into pressure and friction contributions:

$$C_{D_{\mathrm{nf}}} = C_{D_p} + C_{D_f} \ . \tag{6}$$

Differently from the near-field analysis, the far-field analysis provides a physical drag breakdown into viscous, wave, and lift-induced drag components and allows to eliminate spurious (numerical) drag:

$$C_{D_{\mathrm{ff}}} = C_{D_v} + C_{D_w} + C_{D_i} \quad \text{with} \quad C_{D_v} = C_{D_{vp}} + C_{D_f} \ . \tag{7}$$

The viscous pressure drag $C_{D_{vp}}$ is part of the viscous drag that is not due to the friction drag C_{D_f} (i.e. displacement effect, flow separation, etc.). Spurious drag is defined as drag generated through entropy or stagnation enthalpy variations along streamlines outside physical viscous layers and shocks and not resulting from vortex decay. It is generally produced in regions of strong pressure gradients via the addition of artificial dissipation and it is considered purely a numerical artefact. The following near-field/far-field drag balance can be retrieved:

$$C_{D_p} + C_{D_f} = C_{D_v} + C_{D_w} + C_{D_i} + C_{D_{\mathrm{sp}}} \tag{8}$$

$$C_{D_{\mathrm{nf}}} = C_{D_{\mathrm{ff}}} + C_{D_{\mathrm{sp}}} \tag{9}$$

A detailed analysis of the formulations and methods relative to the far-field approach can be found in [42, 43]. In this study, the postprocessing software FFDπ is used at the end of the CFD computation to perform the far-field drag analysis. The FFDπ software uses the Cassiopée library [44] and can handle structured/unstructured grids in parallel environment.

V. Iso-lift comparisons

A. DPW-5 Results using full-hexahedral meshes

1. Choice of numerical parameters

Before performing the grid convergence study, it is important to define the best numerical parameters to be used in CODA. Here, the main focus is to characterize the gradient computation. Depending on the discretization, the reconstruction includes special treatments of variables, like adding a face-gradient correction, or applying a slope limiter, etc. In the following, three types of face-gradient corrections are studied; they are referred to as 'face' , 'edge', and 'cell-to-face' augmentation. The other objective is to understand the influence of the slope limiter in the numerical solution, especially on the aerodynamic coefficients. As explained in [30], convergence issues can become a problem when using limiters that use nondifferentiable functions (such as in Barth and Jespersen [29]). Venkatakrishnan [30]'s limiter is well-suited for unstructured grid applications and also satisfies the theory of total-variation-diminishing (TVD) schemes in one dimension. Since Venkatakrishnan [30]'s limiter presents improvement with respect to the one proposed by Barth and Jespersen [29], only the former is analyzed. In this formulation, the threshold constant K needs to be specified. Low values of K make the scheme more dissipative and the simulation easier to converge, high values of K neutralize the effect of the limiter and, for flows with discontinuities, can cause the solution to diverge. Here, we test three values of $K = 0.1$, 1 and 10.

The results are summarized in Tables 5 and 6. Table 5 gives the angles of attack, near-field drag values, and the pitching-moment coefficients obtained with CODA using different numerical parameters and same grid resolution (L3). The elsA result is also displayed in the table for reference purposes for the same mesh. The medium mesh was chosen because it is representative of current practices for aircraft RANS simulations and presents a good resolution near the wall ($Y^+ \approx 1$). All drag coefficients are given in drag counts (dc, one drag count is 10^{-4}).

Regardless of the type of augmentation ('face', 'edge' or 'cell-to-face'), a good agreement is observed between elsA and CODA results. The impact of the limiter constant K was also investigated. The discrepancies in the drag coefficient between CODA and elsA vary between 0.2 and 4 d.c. (depending on the value of K). Such differences are acceptable taking into consideration the scatterband of 10-15 counts presented in the compiled CFD results from the literature [45]. Moreover, as expected, when K increases, the aerodynamic coefficients approach the reference values. The drag difference between simulation with limiter ($K = 10$) and without limiter is only 0.5 counts. The difference between the pitching moment is negligible. Note that to obtain the simulation without limiter, we had to start the computation from a converged solution run with limiter. Thus, it appears that keeping $K = 10$ offers a good tradeoff between convergence properties and result quality at least for this structured grid. The influence of using the Green-Gauss theorem and the least-squares scheme was also questioned. For this type of structured mesh, the results are very close (same angle of attack, momentum and friction drag coefficients), the sole difference is that using the Green-Gauss scheme, the pressure drag (and hence the total drag) is increased by 0.6 dc. The extGG scheme was also tested and, as discussed in the next section, it can provide improved results. Here, we note that the angle of incidence and drag coefficients are reduced and gets closer to the converged values (see Table 7).

Table 4 presents the far-field analysis and therefore the drag coefficients given by the FFDπ software. The lift and total near- and far-field drag coefficients are given. The latter is then decomposed into viscous pressure, friction, wave and induced drag coefficients. The spurious drag coefficient is the difference between the near-field drag and the far-field drag coefficients. First, it is worth mentioning that the elsA results obtained with the modern FFDπ software compares extremely well with the ones reported in [15] acquired with the well established ffd72 software. This comparison validates the FFDπ module. The agreement between CFD results using elsA and CODA is also remarkable. The far-field drag discrepancy is less than 0.5 d.c. for simulations using linear and limited-linear ($K = 10$) face-augmentation reconstruction when compared to the reference elsA solution. Note that the spurious drag is reduced if the threshold value K is increased. This observation supports the choice of $K = 10$ as optimal value for the present configuration, and this choice is kept for further analysis. Actually, for $K = 10$, $C_{D_{sp}}$ is lower in CODA than in the optimized elsA solution. The drag breakdown is also very close between solvers. The objective of this section was to investigate the impact of numerical parameters on the solution. We noticed that the higher the value of K, the lower is the impact of the limiter (and the numerical diffusion). Even though $K = 10$ is adequate for these structured meshes, high values of K can induce convergence issues when considering other types of meshes.

To complete the previous analysis, we plot in Fig. 3 the pressure and skin-friction coefficient distributions along the chord for three sections located at 50, 75 and 90% of the wingspan (y=14.7, 22.0 and 26.44 m respectively). In general, a good comparison between CODA and elsA is achieved confirming the aforementioned discussion. In the shock region, minimal differences exist.

Case	α	C_L	$C_{D_{\mathrm{nf}}}$	$C_{D_{\mathrm{p}}}$	$C_{D_{\mathrm{f}}}$	C_M
L3-elsA	2.657	0.4998	256.1	142.1	114.0	-0.0883
L3-LS-LL-K0.1-F	2.641	0.5000	260.1	145.8	114.3	-0.0902
L3-LS-LL-K1-F	2.657	0.4999	257.8	144.0	113.8	-0.0887
L3-LS-LL-K10-F	2.672	0.4999	256.4	142.9	113.5	-0.0874
L3-LS-L-F	2.673	0.5000	255.9	142.6	113.3	-0.0873
L3-LS-L-E	2.685	0.4997	255.8	142.5	113.3	-0.0862
L3-LS-L-C2F	2.686	0.4999	255.9	142.5	113.4	-0.0862
L3-stdGG-LL-K10-F	2.672	0.5000	257.0	143.5	113.5	-0.0874
L3-extGG-LL-K10-F	2.630	0.5000	254.8	139.7	115.2	-0.0905

Table 5 Near-field drag breakdown. Comparison between elsA and CODA results using several numerical setups and the L3 grid resolution (full-hexahedral mesh). LS = least-squares, GG = Green Gauss, LL = limited linear, L = linear, K = Venkatakrishnan's constant, F = face, E = edge or C2F = cell-to-face augmentation.

Case	$C_{D_{\mathrm{nf}}}$	$C_{D_{\mathrm{ff}}}$	$C_{D_{\mathrm{f}}}$	$C_{D_{\mathrm{vp}}}$	$C_{D_{\mathrm{w}}}$	$C_{D_{\mathrm{i}}}$	$C_{D_{\mathrm{sp}}}$
L3-elsA	256.1	255.6	114.0	42.4	5.8	93.4	0.7
L3-LS-LL-K0.1-F	260.1	257.5	114.3	44.6	6.2	92.4	2.6
L3-LS-LL-K1-F	257.8	256.8	113.8	44.8	5.5	92.9	1.1
L3-LS-LL-K10-F	256.4	256.1	113.5	43.7	5.7	93.2	0.3
L3-LS-L-F	255.9	255.7	113.3	44.0	5.8	92.6	0.2
L3-LS-L-E	255.9	255.7	113.4	43.3	5.9	93.1	0.2
L3-LS-L-C2F	255.9	255.7	113.3	43.3	5.9	93.2	0.2
L3-stdGG-LL-K10-F	257.0	256.2	113.5	43.7	5.7	93.3	0.8
L3-extGG-LL-K10-F	254.9	254.2	115.1	41.2	5.7	92.2	0.7

Table 6 Far-field drag breakdown at iso-C_L. Comparison between elsA and CODA results using several numerical setups and the L3 grid resolution (full-hexahedral mesh). LS = least-squares, GG = Green Gauss, LL = limited linear, L = linear, K = Venkatakrishnan's constant, F = face, E = edge or C2F = cell-to-face augmentation.

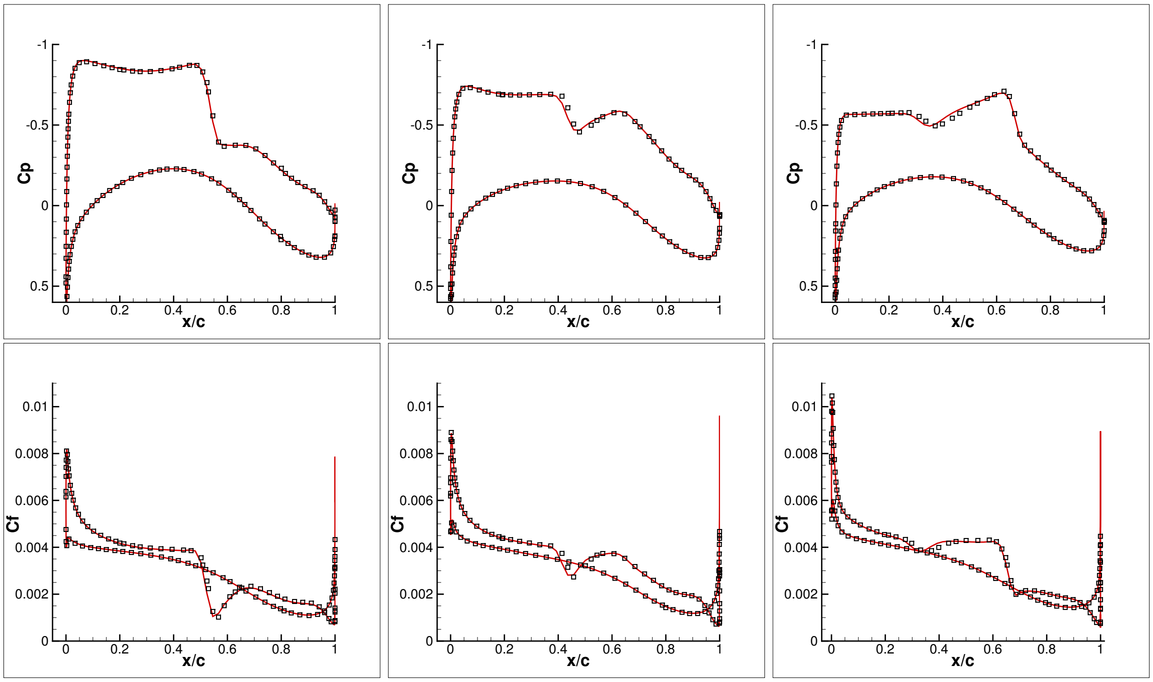

Fig. 3 Numerical pressure (top) and skin-friction (bottom) distributions over the wing section at $y/b = 0.5$ (left), $y/b = 0.75$ (middle) and $y/b = 0.90$ (right). CODA LL-K10-F-LS (line); elsA (symbols). Both cases were run on the same L3 full-hexahedral mesh.

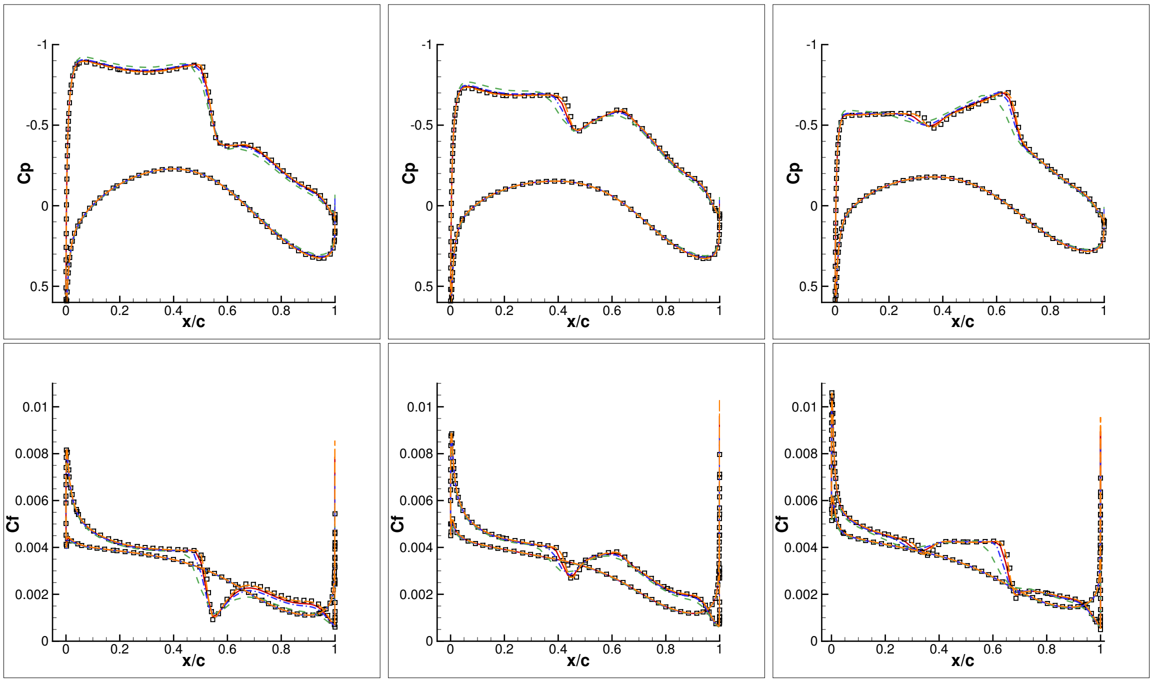

Fig. 4 Grid refinement study. Numerical pressure (top) and skin-friction (bottom) distributions over the wing section at $y/b = 0.5$ (left), $y/b = 0.75$ (middle) and $y/b = 0.90$ (right). CODA (lines) : L1 (green dashed), L2 (blue dash-dotted), L3 (red solid) and L4 (orange long-dashed lines); elsA L5 (symbols).

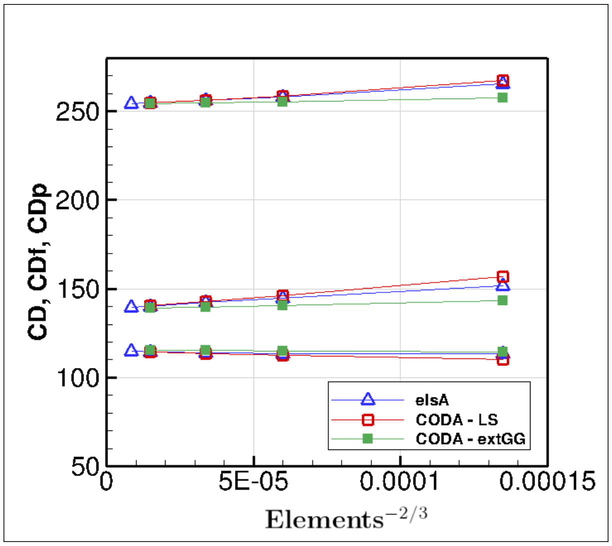

Fig. 5 Grid convergence study for CODA and elsA for the full-hexahedral meshes of DPW-5 at target lift 0.5.

2. Grid convergence Study

Hue [7] showed that the results obtained using grid levels L4-L6 were extremely close, and concluded that the fourth refinement level (17 M elements) was sufficient to evaluate the global aerodynamic forces and moments with a satisfactory precision. For this reason, in this section, only grids L1-L4 are considered. The results are summarized in Tables 7 and 8. Table 7 gives the angles of attack, near-field drag values, and the pitching-moment coefficients obtained with CODA for each grid level. Table 8 presents the far-field analysis and therefore the drag coefficients given by the FFDπ software. For comparison, the elsA results for grid L5 are also shown in these tables. CODA results are displayed using two gradient-computation methods: the least-square, which showed good agreement with elsA in the last section and the extGG method, which is known to be more accurate.

If we consider the CODA results obtained with the LS method, Table 7 shows that a decrease of 12.3 dc is noticed for the total drag coefficient between the coarsest grid L1 and the finest grid L4. This confirms the insufficient discretization properties of the L1 grid. This discrepancy is further reduced to 1.4 d.c. if we consider the L3 grid, which is more acceptable. An interesting point is that the pressure component of the total drag is more sensitive to the mesh resolution than the friction drag, which is in agreement with [7]. If we consider the extGG method, the results are much less affected by the grid resolution in comparison with the LS and elsA results (see Figure 5). The total drag coefficient differs only by 3.2, 0.9 and 0.5 d.c. between grids L1, L2 and L3 with respect to grid L4. This indicates the superior quality of this numerical scheme. As a matter of fact, Figure 5 shows that CODA using the extGG method presents a better convergence than even the well-stablished solver elsA. The converged value of the total drag for the CRM wing-body configuration in these aerodynamic conditions is around 254 dc.

Table 8 shows the far-field drag analysis. A close agreement between Hue [15]'s study using the elsA solver and

Case	α	C_L	$C_{D_{\text{nf}}}$	$C_{D_{\text{p}}}$	$C_{D_{\text{f}}}$	C_M
L1-LS-LL-K10-F	2.822	0.5002	267.3	157.0	110.3	-0.0765
L2-LS-LL-K10-F	2.711	0.4999	258.7	146.2	112.5	-0.0844
L3-LS-LL-K10-F	2.672	0.4999	256.4	142.9	113.5	-0.0874
L4-LS-LL-K10-F	2.645	0.5000	255.0	140.7	114.3	-0.0895
L1-extGG-LL-K10-F	2.678	0.5000	257.4	143.2	114.2	-0.0864
L2-extGG-LL-K10-F	2.639	0.5000	255.3	140.3	115.0	-0.0897
L3-extGG-LL-K10-F	2.630	0.5000	254.8	139.7	115.2	-0.0905
L4-extGG-LL-K10-F	2.625	0.5000	254.4	139.2	115.2	-0.0911
L5-elsA	2.637	0.4995	254.2	139.5	114.7	-0.0899

Table 7 Near-field drag breakdown. Grid convergence study using the full-hexahedral meshes. All computations were performed using LL = limited linear, K = 10, F=face. LS = least-squares method, extGG = extended Green-Gauss.

the present work using CODA is achieved, confirming the reproducibility of the results. We note that the viscous pressure drag contribution is greatly affected by the level of grid refinement. The spurious drag is also reduced when the grid is refined. The wave and induced drag seem to be predicted with a satisfactory accuracy from the second level of refinement. For the grid-converged solution, the far-field approach gives the following drag partition: the viscous drag represents 62% of the total drag (74% of C_{D_v} are due to the friction drag, and the remaining 26% come from the viscous pressure drag). The wave drag corresponds to only 2% of the drag, while the lift-induced drag is responsible for 36% of the aircraft drag. Note that when the extGG method is used, the spurious drag is more accentuated than when the LS method is active. However, the far-field analysis shows that it is possible to predict the converged value of the total drag using a mesh of only 5M elements (L3 resolution), which is an outstanding result.

Figure 4 exhibits the pressure and skin-friction distributions along the chord at 50, 75 and 90% of the wingspan for the four grids used in this study together with the elsA solution for the L5 grid. Discrepancies appear especially in the region close to the shock position. It seems clear that the refinement level of L1 is not sufficient to produce a satisfactory resolution of the flowfield; the shock description is not accurate, and there are oscillations close to the trailing edge. Disagreements between results are reduced when the grid refinement is improved. Note that results obtained using grids L4 are very close to the elsA solution using a finer grid resolution (L5). The poor quality of mesh L1 makes it an ideal candidate to validate high-order schemes. This test is presented in the next section.

3. Discontinuous Galerkin formulation

In this section, the benefits of using the high-order DG method described in III.A.2 with respect to the classical FV Roe scheme are investigated. This approach allows enhancing the accuracy by increasing the degree of the polynomial approximation of the solution in the control volumes. Table 9 reports simulation results obtained with a third-order (polynomial degree $p = 2$) CODA DG scheme on a coarse grid (mesh L1) together with reference results obtained

Case	$C_{D_{\mathrm{nf}}}$	$C_{D_{\mathrm{ff}}}$	$C_{D_{\mathrm{f}}}$	$C_{D_{\mathrm{vp}}}$	$C_{D_{\mathrm{w}}}$	$C_{D_{\mathrm{i}}}$	$C_{D_{\mathrm{sp}}}$
L1-LS-LL-K10-F	267.2	264.5	110.3	53.0	6.7	94.6	2.7
L2-LS-LL-K10-F	258.7	258.1	112.5	46.2	5.9	93.5	0.6
L3-LS-LL-K10-F	256.4	256.1	113.5	43.7	5.7	93.2	0.3
L4-LS-LL-K10-F	255.0	254.8	114.3	42.1	5.6	92.8	0.2
L1-extGG-LL-K10-F	257.7	256.2	114.2	44.8	6.1	91.1	1.5
L2-extGG-LL-K10-F	255.4	254.5	115.0	42.3	5.8	91.4	0.9
L3-extGG-LL-K10-F	254.9	254.2	115.1	41.2	5.7	92.2	0.7
L4-extGG-LL-K10-F	254.6	254.2	115.2	41.1	5.8	92.1	0.4
L5-elsA	254.2	254.2	114.7	40.9	5.7	92.8	0.1

Table 8 Far-field drag breakdown at iso-C_L. Grid convergence study using the full-hexahedral meshes. All computations were performed using LL = limited linear, K = 10, F=face. LS = least-squares method, extGG = extended Green-Gauss.

Simulation	α	C_L	$C_{D_{\mathrm{nf}}}$	$C_{D_{\mathrm{p}}}$	$C_{D_{\mathrm{f}}}$	C_M
L1-DG-o3	2.637	0.4993	254.7	141.2	113.5	-0.0898
L4-LS-LL-K10-F	2.645	0.5000	255.0	140.7	114.3	-0.0895
L4-extGG-LL-K10-F	2.625	0.5000	254.4	139.2	115.2	-0.0911
L5-elsA	2.637	0.4995	254.2	139.5	114.7	-0.0899

Table 9 Near-field drag breakdown. Comparison between elsA and CODA results using the FV/DG discretization and full-hexahedral meshes.

using a second-order FV schemes using CODA (L4) and elsA (L5). Results are found to be very accurate with the DG approach on the coarse L1 mesh. The level of accuracy of this CODA DG simulation is comparable to the FV CODA and elsA results using the finest meshes L4/L5. This shows the ability of DG schemes to obtain good accuracy on coarse meshes, by increasing the polynomial degree, which is done easily as this parameter is specified by the user. This method is therefore very convenient for any user or applied engineer, since it avoids time consuming mesh regeneration. In addition, computational storage can be reduced since this methodology allows us to use coarser meshes. For instance, while mesh L4 has 17.2 M DoF, simulation L1-DG-o3 involves around 6.4M DoF and results are as accurate as the ones obtained with the FV methods using CODA on grid L4. It is important to highlight that preliminary computations with lower polynomial degree are required to enable the convergence of the L1-DG-o3 ($p = 2$) simulation. As shown in figure 6, solutions obtained with the DG (L1-DG-o3, contour lines) and the FV (L4-extGG-LL-K10-F, color) approaches yield same results (wall pressure coefficient). In VI.B, we investigate in more detail the DG approach using a full-tetrahedral unstructured mesh.

B. DPW-6 Results using mixed-unstructured meshes

In this section, we perform simulations of the CRM geometry from the DPW-6. Unlike the original CRM configuration used in DPW-5, the wing shape was corrected to take into account the aeroelastic twist and bending that

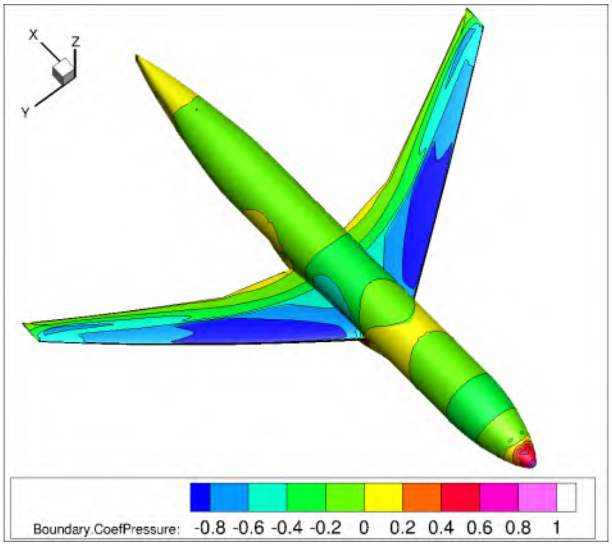

Fig. 6 Wall-pressure coefficient for simulation using the DG (L1-DG-o3) and FV (L4-extGG-LL-K10-F) formulations. DG result is displayed as iso-contour lines and FV result as colored map.

were measured in the wind tunnels. Results obtained with CODA, elsA and TAU on different grids are compared. The elsA results were computed using overset grids with an average Y^+ at the wall lower than one [13]. The reference elsA simulation was performed on a mesh containing 58.2 M elements (WB5) [13], while TAU simulation was performed using a 39.7 M node mesh (F) [46]. CODA simulations were carried out with mixed unstructured grids, with 27.9 M and 53.2 M elements for the coarse (UM1) and the fine (UM2) levels, respectively, as defined in Table 3. Similarly to the analysis performed on structured grids in the section V.A, we study the drag impact of standard and extended Green-Gauss gradient computations for the convective fluxes and the type of face-gradient augmentation (face, edge and cell-to-face) for the diffusive fluxes.

The near-field drag breakdown is given on Table 10. It was shown previously that the extGG element gradients are more accurate than stdGG element gradients. The difference between the two approaches is even more salient for mixed unstructured grids with a near-field drag coefficient increment of 11.7 dc. In the following, we keep the extGG gradients as the gradient parameter. It is also known that the edge (E) augmentation of face gradients is more accurate than the others, especially for strongly non-smooth meshes. Here, we intend to test the three types of face-gradient augmentations on high-quality unstructured meshes. Simulations using the extGG gradients and F/E/C2F-augmentations give close results in terms of drag. The difference between the reference elsA solution and the CODA results is less than 0.5 dc as long as extGG gradients are employed, which is excellent if we take into consideration the discrepancy of around 10 counts presented in the compiled CFD results from the literature on the finest meshes using the SA turbulence model [6]. Therefore, for this type of regular unstructured mesh, the choice of face-gradient augmentation is minor. We also used a finer mesh (UM2) to evaluate resolution effects. The results obtained with grids UM1 and UM2 are very close (same angle of attack, momentum and friction drag coefficients), the sole difference is that the pressure drag (and hence the

Simulation	α	C_L	$C_{D_{\mathrm{nf}}}$	$C_{D_{\mathrm{p}}}$	$C_{D_{\mathrm{f}}}$	C_M
WB5-elsA [13]	2.428	0.5001	253.4	138.5	114.9	-0.0964
F-TAU [46]	2.372	0.5000	256.5	141.5	115.0	-0.101
UM1-stdGG-LL-K10-F	2.438	0.4999	265.5	150.8	114.7	-0.0972
UM1-extGG-LL-K10-F	2.400	0.4998	253.8	138.1	115.7	-0.0986
UM1-extGG-LL-K10-E	2.416	0.5000	254.3	138.5	115.8	-0.0979
UM1-extGG-LL-K10-C2F	2.416	0.5000	254.3	138.5	115.8	-0.0979
UM2-extGG-LL-K10-F	2.400	0.4998	253.6	137.9	115.7	-0.0986

Table 10 Near-field drag breakdown. Comparison between elsA (overset grid), TAU (mixed unstructured) and CODA (UM1 and UM2) results using several numerical setups and grid resolutions (mixed-unstructured mesh). stdGG = standard Green Gauss and extGG = extended Green-Gauss, LL = limited linear, K = Venkatakrishnan's constant, F = face, E = edge or C2F = cell-to-face augmentation

Case	$C_{D_{\mathrm{nf}}}$	$C_{D_{\mathrm{ff}}}$	$C_{D_{\mathrm{f}}}$	$C_{D_{\mathrm{vp}}}$	$C_{D_{\mathrm{w}}}$	$C_{D_{\mathrm{i}}}$	$C_{D_{\mathrm{sp}}}$
WB5-elsA [13]	253.4	253.7	114.9	41.6	5.7	91.5	-0.3
UM1-stdGG-LL-K10-F	265.5	255.7	114.7	43.1	6.0	91.9	9.8
UM1-extGG-LL-K10-F	254.4	254.9	115.7	41.5	5.8	91.9	-0.5
UM1-extGG-LL-K10-E	254.9	255.4	115.8	41.7	6.0	91.9	-0.5
UM1-extGG-LL-K10-C2F	254.9	255.4	115.8	41.7	6.0	91.9	-0.5
UM2-extGG-LL-K10-F	254.3	254.6	115.7	41.2	5.6	92.0	-0.3

Table 11 Far-field drag breakdown at iso-C_L. Comparison between elsA (overset mesh) and CODA results using several numerical setups (mixed-unstructured mesh). stdGG = standard Green Gauss and extGG = extended Green-Gauss, LL = limited linear, K = Venkatakrishnan's constant, F = face, E = edge or C2F = cell-to-face augmentation.

total drag) is decreased by 0.2 dc. We highlight that CODA results obtained with extGG gradients lie between those obtained with elsA and TAU, keeping in mind that TAU simulations presented in [46] are known to be not fully mesh converged.

The far-field drag coefficient obtained with elsA using an overset mesh and with CODA using mixed unstructured meshes are within 2 dc (Table 11). Results obtained with the fine mesh (UM2) are closer to the elsA reference compared with the coarse mesh (UM1). This can be explained by a lower wave drag $C_{D_{\mathrm{w}}}$, indicating that the shock region is better represented and a lower spurious drag $C_{D_{\mathrm{sp}}}$, due to the better discretization. As expected, the largest discrepancy arises when using stdGG element gradients showing a difference of more than 12 dc between CODA and elsA for the near-field drag. However, the far-field breakdown reports a discrepancy of only 2 dc demonstrating that the far-field drag analysis is able to detect the large amount of spurious drag inherent in this discretization scheme. The impact of the face-gradient augmentation is not problematical, since the $C_{D_{\mathrm{ff}}}$ results employing the F, E or C2F augmentation differ by only 0.5 dc. This proves the good quality of the mesh. We recall that for meshes with high skewness and/or aspect ratio, the use of edge augmentation is recommended.

		CODA stdGG			CODA extGG			TAU		
Level	Name	AoA	CL	CD	AoA	CL	CD	AoA	CL	CD
L1	Tiny	2.706	0.58003	283.45	2.665	0.58006	269.81	2.6714	0.57991	273.69
L2	Coarse	2.713	0.58008	280.25	2.671	0.57999	269.24	2.6781	0.57996	272.25
L3	Medium	2.716	0.58001	278.31	2.676	0.58005	269.00	2.6888	0.57991	271.60
L4	Fine							2.6899	0.57993	271.03
L5	Extra-fine	2.718	0.58000	275.86	2.684	0.57999	268.91	2.6926	0.57996	270.68
L6	Ultra-fine							2.6938	0.58006	270.48

Table 12 DPW-7, case 1a (target lift 0.58): CODA vs TAU, angle of attack and drag coefficient

C. DPW-7 Results using unstructured meshes

Here, the unstructured DPW-7 meshes described in Sec. II are considered (cf. Table 4) to compare CODA with TAU. Namely, case 1a of the DPW-7 is considered for a comparative mesh convergence study, where a target lift coefficient of 0.5800 ±0.0001 at Mach 0.85 is considered for a Reynolds number of 20M. Table 12 lists the angle-of-attack values found for CODA and TAU that result in a target lift value of 0.5800 ±0.0001. In general, the finer the mesh, the larger is the angle of attack. Note here that for CODA, the DoF is linear in the number of cells/elements (cell-centered metric), whereas for TAU, the discrete solution lives at the nodes of the mesh (node-centered metric). For this reason, computing the flow solution using the Tiny, Coarse and Medium grids with CODA is enough to perform comparison with TAU for similar grid resolution. The Extra-fine grid was also computed to confirm the linear behaviour of drag components toward estimated mesh-converged values. As can be seen from these values, when using the stdGG gradients, the angle of attack is larger than for CODA with extGG gradients or TAU. As expected, this results in larger drag values for this version (CODA stdGG gradients) than for the other two. The resulting drag coefficients are presented in Fig. 7 together with linear fits to estimate the mesh-converged values. All three variants agree in a viscous drag of about 95 dc, almost independent of how fine the meshes are. We recall that the boundary-layer mesh is hexahedral-dominant, so that cell-centered stencil and node-centered stencil are quite similar in these regions of the flow. Concerning the pressure drag, however, CODA with stdGG gradients (estimated mesh-converged value of about 179.8 counts) deviates significantly from the other two, namely CODA with extGG gradients (about 173.5 counts) and TAU (175.0 counts). Moreover, stdGG gradients for CODA result in a significantly increased rate of change of (pressure) drag w.r.t. mesh size. Actually, using extGG gradients with CODA seems even slightly less affected by (too) coarse meshes than TAU, thanks to the quite large stencil. The estimated mesh-converged total drag for CODA with extGG gradients is in fact 1.3 counts smaller than the one for TAU. As a conclusion of these results, using the extGG gradients comes with a significantly increased accuracy, allows for using relatively coarse meshes. Clearly, this comes at an increased cost (in runtime for gradient computation). For steady-state simulations using implicit time integration, however, this seems minor compared to what is gained (according to our experiences so far). The CODA results obtained with extGG gradients agree notably well with the TAU reference results in the DPW-7 (case 1a) setting considered here.

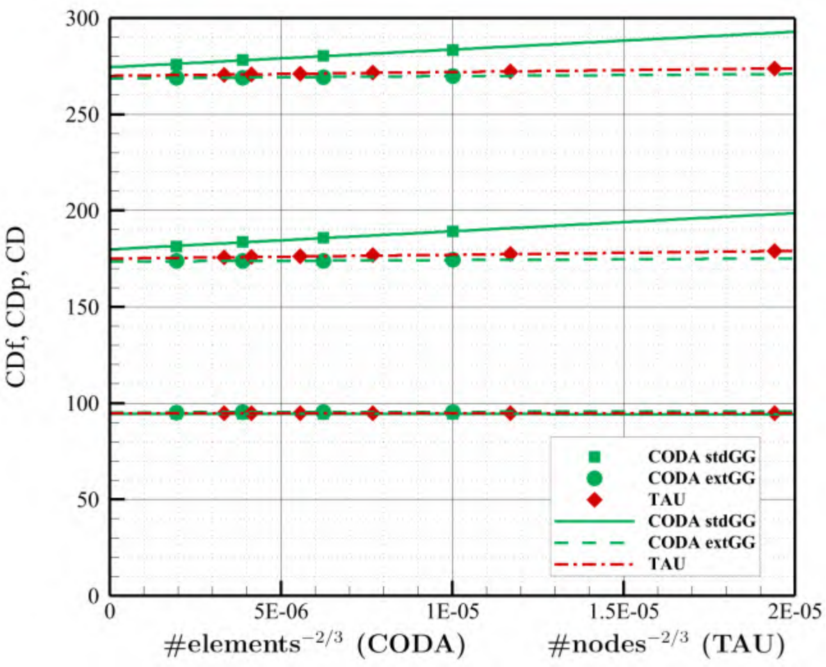

Fig. 7 Grid convergence study for CODA and TAU for DPW-7 case 1a, namely drag for target lift 0.58

VI. Comparisons at fixed angle of attack

A. DPW-5 Results using mixed-unstructured meshes

In this section, the accuracy of CODA is assessed in the context of mixed-unstructured meshes composed of hexahedra only (hexa meshes) and tetrahedrons and prisms (hybrid meshes), with an emphasis on the mesh convergence properties of the FV numerical schemes compared to the TAU solver on same meshes to keep the effects of the grid properties on the comparison small. Note that the number of elements determine the number of DoF for the cell-centered code CODA and the number of nodes determine the number of DoF for the node-centered code TAU. For the considered hybrid meshes the number of elements is significantly larger than the number of nodes, Table 2. The CRM configuration considered is the one proposed for the DPW-5. The flow conditions are: Mach 0.85, Reynolds 5 million based on reference chord, and Prandlt number 0.72. Different to case 1 defined in the DPW-5 a fixed angle of attack of 2.209 degrees is used for the mesh convergence study to assess the effect on drag and lift coefficients of the numerical schemes used.

The main focus is to characterize CODA's stdGG and extGG element gradient computations for mixed-unstructured meshes. The face-gradient augmentation is set to 'edge'. All six equations are treated as a coupled system, using Roe's upwinding scheme (with the default entropy-fix fraction of 10%). Second order (in space) is achieved via limited linear reconstruction using the corresponding gradient computation and the 'spline quintic' limiter variant with $K = 5.0$. In the following results computed with extGG and stdGG gradients on both the hexahedra and hybrid mesh families are compared to results of the TAU solver. For TAU, also all six equations are discretized by a second-order central scheme

hexa	L1	L2	L3	L4	L5	mesh-converged
CODA stdGG	256.87	252.79	252.56	252.92	253.17	253.32
CODA extGG	251.36	252.88	253.49	253.84	253.91	254.07
TAU	245.68	250.27	251.47	252.73	253.16	253.74
hybrid	**L1**	**L2**	**L3**	**L4**	**L5**	**mesh-converged**
CODA stdGG	281.18	271.39	267.71	263.31	261.28	261.33
CODA extGG	254.82	254.47	254.37	254.10	254.02	254.05
TAU	249.06	252.02	253.21	253.62	253.74	253.93

Table 13 Comparison of near-field total drag obtained on DPW-5 hexa and hybrid meshes.

with matrix dissipation.

Total drag and lift coefficients are considered at grid levels L1 to L5 on DPW-5 hexa and hybrids grids for both TAU and CODA. For CODA, the coefficients are analyzed using extGG and stdGG gradients. In table 13, the near-field total drag for the meshes from L1 to L5 is given. The estimated mesh-converged drag values computed by fitting the drag values obtained on meshes with more than 2.8 M elements/nodes (hexa L3-L5, hybrid L1-L5) to a linear function using the standard least-squares algorithm are given too. For the hexa meshes CODA stdGG, CODA extGG and TAU estimated mesh-converged values are in the range of 0.75 counts. CODA stdGG convergence is monotone indicating a higher discretization error on coarser grids. CODA extGG and TAU convergences are strictly monotone. Note that CODA extGG presents better convergence properties than TAU, e.g. difference of drag between L3 and estimated mesh-converged drag is 0.58 counts for CODA extGG and 2.27 counts for TAU, indicating that CODA extGG entails lower discretization errors on coarser meshes. A possible explanation for this is extGG gradients use a least-squares gradient-based, piecewise linear reconstruction to compute values at face integration-points different to the standard approach and node-centered schemes, which interpolate these values linearly between element-averaged values of the neighbouring elements of a face. For the hybrid meshes CODA extGG and TAU estimated mesh-converged values are in the range of 0.12 counts, whereas CODA stdGG estimated mesh-converged drag is more than 7 counts higher. These relatively large differences can be related to the interpolation error introduced by stdGG gradients, which reduces the order of the discretization in particular on non-smooth, mixed-elements grids. On the coarsest hybrid mesh L1, CODA extGG differs only by 0.77 counts form the result on the finest grid L5. For TAU this difference is more than six times higher. A possible explanation for this, besides the more accurate computation of values at face integration-points, is related to the fact that, on the hybrids grids, the cell-centered FV scheme has a higher number of DoF than a node-based FV scheme. Finally, the difference between the estimated mesh-converged drag for hexa and hybrid meshes is 0.02 counts for CODA extGG and 0.19 for TAU, indicating that the CODA extGG result is less grid sensitive.

The lift computed using meshes L1 to L5 are displayed in table 14, together with the estimated mesh-converged values. The latter was estimated by fitting the lift values obtained on meshes with more than 2.8 M elements/nodes (hexa L3-L5, hybrid L1-L5) to a linear function using the standard least-squares algorithm. As the near-field drag results

hexa	L1	L2	L3	L4	L5	mesh-converged
CODA stdGG	0.4848	0.4971	0.5018	0.5053	0.5066	0.5082
CODA extGG	0.5000	0.5052	0.5071	0.5084	0.5087	0.5093
TAU	0.4876	0.5000	0.5027	0.5059	0.5070	0.5085
hybrid	L1	L2	L3	L4	L5	mesh-converged
CODA stdGG	0.4771	0.4918	0.4989	0.5037	0.5059	0.5093
CODA extGG	0.4985	0.5052	0.5074	0.5083	0.5086	0.5097
TAU	0.4905	0.5027	0.5062	0.5078	0.5082	0.5089

Table 14 Comparison of lift obtained on DPW-5 hexa and hybrid grids.

indicate, CODA stdGG is prone to higher discretization errors. Therefore, only CODA extGG and TAU results are discussed. CODA extGG and TAU estimated mesh-converged lift values are in the range of 0.08 counts on both hexa and hybrid meshes. On each mesh level from L1 to L4 the difference in lift compared to the finest grid L5 is lower for CODA extGG compared to TAU on both hexa and hybrid grids. Note that lift obtained by CODA extGG on grid levels L2 to L5 is almost the same on hexa and hybrids grids. The difference in the lift coefficient between CODA extGG and TAU is reduced if compared to the difference in the drag. It appears that the number of DoF affects less the lift coefficient than the drag coefficient, due to same distribution of DoF in the boundary layer normal to the surface for both hexahedral and hybrids grids. The difference between the lift on the finest hexa and hybrid grids is 0.01 counts for CODA extGG and 0.12 for TAU indicating that CODA extGG is less grid sensitive.

Figure 8 shows lift (top left), total drag (top right), pressure drag (bottom left), and friction drag (bottom right). Note that the coefficients are shown against number of elements for CODA and number of nodes for TAU to represent the number of DoF used for cell-centered and node-centered grid-metric and that the tetrahedra of the hybrid grids result from decomposition of hexahedra of the hexa meshes outside the boundary layer, i.e. most of the additional DoF for cell-centered are located towards the farfield, probably without effect on accuracy. Comparing pressure and friction contribution of total drag clarifies that the discretization error observed for CODA stdGG is mainly related to the pressure distribution. Furthermore, Figure 8 shows that TAU results on hexa and hybrid grids are different, although the number of DoF is identical for both types of grids. The difference is related to the computational finite-volumes generated by the node-centered grid-metric. For hybrid grids computational finite-volumes contain more faces than for hexa grids due to the different connectivity of nodes, resulting in a different spatial discretization. Hence, the difference of the TAU results indicate that the magnitude of the discretization error for a mesh level is at least as large as the difference between the results on hexa and hybrid grid of this level. Overall, we can conclude from this grid convergence study, that CODA stdGG discretization is prone to higher discretization errors, whereas the CODA extGG discretization yields improved accuracy compared to TAU on both hexa and mixed-element meshes.

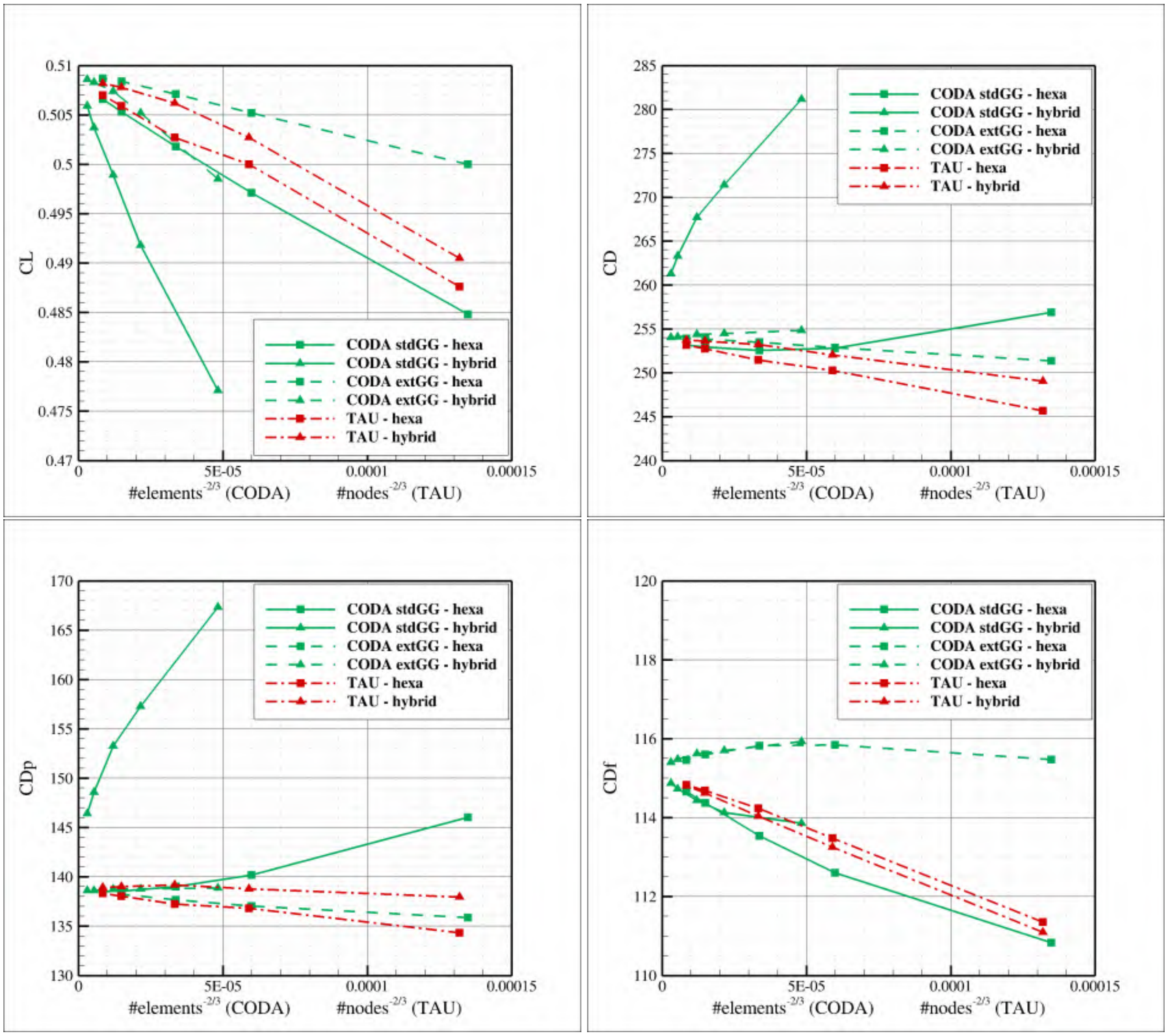

Fig. 8 **C_L (top left), C_D (top right), C_{D_P} (bottom left) and C_{D_F} (bottom right) coefficients for the mesh convergence study related to the DPW-5 CRM configuration. CODA stdGG and extGG results are compared to the reference TAU solutions.**

B. DPW-6/HOW-5 Results using fully tetrahedral unstructured meshes

In this section the accuracy of CODA is assessed in the context of fully unstructured meshes composed of tetrahedra only, with an emphasis on the mesh convergence properties of high-order DG, namely the third order DGp2 scheme. For providing insight on the behavior of the different numerical schemes in CODA, FV and second-order DGp1 computations are also performed on the same meshes. Note that the DGp1 solutions are used as initial conditions for DGp2 simulations. Regarding the FV scheme considered, we use the 'edge' face-gradient augmentation and extGG variant for the reconstruction, the entropy fix fraction value was set to 0.1 and the Venkatakrishnan limiter constant was K=5. The CRM configuration considered is the one proposed for the HOW-5, namely the wing-body variant with a geometry featuring a 2.75 degree aeroelastic deflection. This configuration also corresponds to the third DPW-6 test case. The flow conditions are the following: angle of attack 2.75 degrees, Mach 0.85, Reynolds 5 million based on reference chord, and Prandlt number 0.72. The SA-neg RANS model is used with a freestream eddy viscosity ratio set to 3.0. The HOW-5 has seen groups performing simulations using high-order SUPG finite-element techniques on several meshes. In this work, to evaluate CODA's accuracy, we take as reference the results obtained with the codes COFFE [47] and HOMA [48]. In the present study, we consider 4 meshes over the series of 9 meshes proposed in the HOW-5 website, chosen in a way that the number of elements is doubled for each successive mesh. The details of the meshes and the corresponding number of DoF for FV (second order), DGp1 (second order) and DGp2 (third order) discretizations are summarized in table 15. Figure 9 presents the mesh convergence of the drag and lift coefficients for the simulations performed.

Regarding the drag coefficient, the CODA FV and DGp1 simulations are relatively close in terms of range of values, and those values are above the reference results, although a mesh convergence is observed. Note that the meshes considered here are coarse and in order to fully check the convergence of the FV and DGp1 discretizations, finer meshes should be considered. The CODA DGp1 displays values closer to the SUPGp2 results and overall a better accuracy compared to CODA FV. The accuracy improvements when switching to high order in this case are important, as the CODA DGp2 drag results are very close to the reference SUPGp2 simulations even on the coarser meshes. We also observe a quick mesh convergence to a plateau value of C_D for the DGp2 scheme.

With respect to the lift coefficient, the CODA DGp1 and DGp2 simulations show a monotonic mesh convergence towards the SUPGp2 reference values. The CODA FV simulations are less monotonic regarding mesh convergence for the lift, but the values are still close to the CODA DG results. Overall, CODA's accuracy for FV and DG is found to be satisfactory for these challenging fully unstructured meshes, with second order schemes (DGp1 and FV). CODA DGp2 simulations improve significantly the prediction of the drag, and displays results on par with SUPGp2 references, on coarser meshes. Note that the present discussion focused on spatial accuracy and did not include the FV and DG solvers efficiency, which should be addressed in future work and discussions. Also, on a given mesh, increasing the order of accuracy of DG schemes increases as well the number of DoF per element, and the corresponding impact on

	Mesh L2	Mesh L3	Mesh L4	Mesh L6
#Tetrahedra	515,477	1,073,020	1,920,020	4,776,832
#DoF-FV	515,477	1,073,020	1,920,020	4,776,832
#DoF-DGp1	2,061,908	4,292,080	7,680,020	19,107,328
#DoF-DGp2	5,154,770	10,730,200	19,200,200	47,768,320

Table 15 Mesh properties for the FV and DG CODA simulations of the HOW-5 high-speed CRM case.

the efficiency should be assessed.

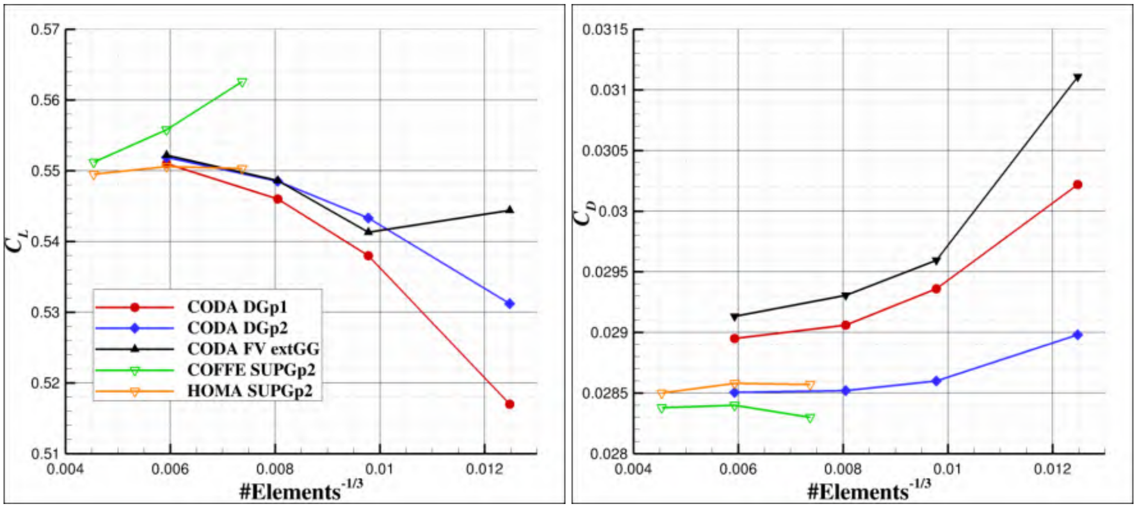

Fig. 9 Lift and drag coefficients mesh convergence study for the 5th High-Order Workshop CRM configuration. DG and FV CODA results are compared to reference SUPG codes.

VII. Conclusion and future steps

In this paper, we compared the new CFD software of ONERA, DLR and Airbus with legacy solvers elsA and TAU. We discuss its numerical schemes and its new capabilities. We perform tests on a disclosed aircraft geometry that is representative of an industrial configuration: the NASA Common Research Model from the Drag Prediction Workshops. Results indicate good accuracy of the new software on both structured and unstructured meshes. We showed that FV results for CODA obtained with standard Green-Gauss gradients are equivalent to those from elsA on full-hexahedral meshes. The accuracy could even be improved on coarser, full-hexahedral meshes using extended Green-Gauss gradients. On mixed-unstructured meshes we also observed improved accuracy for CODA using extended Green-Gauss gradients compared to the legacy solver TAU. We also showed that the standard Green-Gauss gradients applied to the cell-centered grid metric of CODA decreases accuracy on mixed-unstructured, non-smooth meshes in comparison to TAU and the extended Green-Gauss gradient approach. Overall, using the extended Green-Gauss gradients provides an increased accuracy compared to the legacy solvers elsA and TAU on coarse grids, whereas the asymptotic results are comparable. We focused on the spatial discretizations provided by CODA to assess the capabilities of the software with a particular emphasis on accuracy over optimizing computational performance. Of course, the extended gradient approach comes with an increased cost in runtime, which seems to be acceptable if coarser meshes can be used to achieve the desired accuracy.

One important feature of CODA is that it includes high-order schemes based on the Discontinuous Galerkin method. The DG approach proved its interest, as the DG simulation using the coarsest hexahedral grid L1 with a third-order accurate scheme (i.e. a quadratic $p = 2$ polynomial approximation in each cell) showed excellent agreement with the elsA reference using a second-order finite-volume scheme using the finest grid L5, and a more accurate result compared to the CODA second-order finite-volume simulation on the same L1 mesh. This example shows the ability of high-order DG schemes to provide enhanced accuracy compared to traditional second order FV schemes on an equivalent mesh, even when considering complex flow physics and geometries. Advantages of DG schemes were further shown from the DPW-6/HOW-5 simulations on fully unstructured meshes (composed of tetrahedra only). The high-order DG approach shows a remarkable robustness to variations in mesh elements type, as the drag prediction for DG $p = 2$ schemes is very accurate even on the coarsest meshes, while the mesh convergence of drag is slower for second order schemes, either finite volume or DG $p = 1$. Globally, the results are encouraging.

The selection of code-to-code studies presented in this paper illustrates on-going CODA verification activities against legacy CFD codes currently in operation. These studies are carried out with the aim of eventually replacing them with a unique software, CODA, in the applied aerodynamics departments of ONERA and DLR as well as in the Airbus design office to fulfill their respective needs. Regarding the deployment of CODA in the industrial context of Airbus, it is essential to recover in the short term the existing capabilities of our well-established finite-volume based solvers. This will ensure a smooth migration towards this unique flow solver, while retaining all other components of existing end-to-end CFD workflows unchanged, pre-processing and post-processing, in particular mesh generation procedures. New practices and guidelines are being elaborated to deal with the impact of the transition from node-centered (TAU) to cell-centered discretization with effects on accuracy and computational performance and from structured multiblock (elsA) to unstructured data layout with effects on computational performance. The other challenge is to make the most of the potential offered by high order DG methods for RANS simulations of aircraft configurations of equivalent complexity in order to take a further step in their accuracy and efficiency, possibly up to eventually supersede finite-volume methods. Building on this partnership, CODA will serve the ambitions of the European aerospace industry for the coming decades and in particular will significantly contribute to the design of next-generation fuel-efficient aircraft.

Acknowledgments

Parts of the work presented here have received funding from the European Union's Horizon 2020 research and innovation program under grant agreement No. 956104 ("NextSim") or the French Directorate General for Civil Aviation (DGAC) project "LAMA".

We kindly thank Stefan Keye (DLR) and David Hue (ONERA) for providing reference solutions using TAU (DPW-7 case 1a) and elsA, respectively.

References

[1] Cary, A. W., Chawner, J., Duque, E. P., Gropp, W., Kleb, W. L., Kolonay, R. M., Nielsen, E., and Smith, B., "CFD Vision 2030 Road Map: Progress and Perspectives," *AIAA Aviation 2021 Forum*, 2021. URL `https://doi.org/10.2514/6.2021-2726`.

[2] Vassberg, J., Dehaan, M., Rivers, M., and Wahls, R., "Development of a common research model for applied CFD validation studies," *26th AIAA applied aerodynamics conference*, 2008, p. 6919. URL `https://doi.org/10.2514/6.2008-6919`.

[3] Rivers, M. B., and Dittberner, A., "Experimental investigations of the NASA common research model," *Journal of Aircraft*, Vol. 51, No. 4, 2014, pp. 1183–1193. URL `https://doi.org/10.2514/1.C032626`.

[4] Ueno, M., Kohzai, M., Koga, S., Kato, H., Nakakita, K., Sudani, N., and Nakamura, Y., "Normalization of wind-tunnel data for NASA common research model," *Journal of Aircraft*, Vol. 52, No. 5, 2015, pp. 1535–1549. URL `https://doi.org/10.2514/1.C032989`.

[5] Cartieri, A., Hue, D., Chanzy, Q., and Atinault, O., "Experimental investigations on common research model at ONERA-S1MA-drag prediction workshop numerical results," *Journal of Aircraft*, Vol. 55, No. 4, 2018, pp. 1491–1508. URL `https://doi.org/10.2514/1.C034414`.

[6] Tinoco, E. N., Brodersen, O. P., Keye, S., Laflin, K. R., Feltrop, E., Vassberg, J. C., Mani, M., Rider, B., Wahls, R. A., Morrison, J. H., et al., "Summary data from the sixth AIAA CFD drag prediction workshop: CRM cases," *Journal of Aircraft*, Vol. 55, No. 4, 2018, pp. 1352–1379. URL `https://doi.org/10.2514/1.C034409`.

[7] Hue, D., "Fifth Drag Prediction Workshop: Computational Fluid Dynamics Studies Carried Out at ONERA," *Journal of Aircraft*, Vol. 51, No. 4, 2014, pp. 1295–1310. URL `https://doi.org/10.2514/1.C032054`.

[8] Sclafani, A. J., Vassberg, J. C., Winkler, C., Dorgan, A. J., Mani, M., Olsen, M. E., and Coder, J. G., "Analysis of the Common Research Model Using Structured and Unstructured Meshes," *Journal of Aircraft*, Vol. 51, No. 4, 2014, pp. 1223–1243. URL `https://doi.org/10.2514/1.C032411`.

[9] Murayama, M., Yamamoto, K., Hashimoto, A., Ishida, T., Ueno, M., Tanaka, K., and Ito, Y., "Japan Aerospace Exploration Agency Studies for the Fifth AIAA Drag Prediction Workshop," *Journal of Aircraft*, Vol. 51, 2014, pp. 1244–1267. URL `https://doi.org/10.2514/1.C032647`.

[10] Park, M. A., Laflin, K. R., Chaffin, M. S., Powell, N., and Levy, D. W., "CFL3D, FUN3D, and NSU3D contributions to the fifth drag prediction workshop," *Journal of Aircraft*, Vol. 51, No. 4, 2014, pp. 1268–1283. URL `https://doi.org/10.2514/1.C032613`.

[11] Ceze, M., and Fidkowski, K. J., "Drag prediction using adaptive discontinuous finite elements," *Journal of Aircraft*, Vol. 51, No. 4, 2014, pp. 1284–1294. URL `https://doi.org/10.2514/1.C032622`.

[12] Konig, B., and Fares, E., "Validation of a Transonic Lattice-Boltzmann Method on the NASA Common Research Model," *54th AIAA Aerospace Sciences Meeting*, 2016, p. 2023. URL `https://doi.org/10.2514/6.2016-2023`.

[13] Hue, D., Chanzy, Q., and Landier, S., "DPW-6: drag analyses and increments using different geometries of the common research model airliner," *Journal of Aircraft*, Vol. 55, No. 4, 2018, pp. 1509–1521. URL `https://doi.org/10.2514/1.C034139`.

[14] Rivers, M., Hunter, C., and Campbell, R., "Further investigation of the support system effects and wing twist on the NASA common research model," *30th AIAA Applied Aerodynamics Conference*, 2012, p. 3209. URL `https://doi.org/10.2514/6.2012-3209`.

[15] Hue, D., "Fifth drag prediction workshop: ONERA investigations with experimental wing twist and laminarity," *Journal of Aircraft*, Vol. 51, No. 4, 2014, pp. 1311–1322. URL `https://doi.org/10.2514/1.C032438`.

[16] Keye, S., Brodersen, O., and Rivers, M. B., "Investigation of aeroelastic effects on the NASA common research model," *Journal of Aircraft*, Vol. 51, No. 4, 2014, pp. 1323–1330. URL `https://doi.org/10.2514/1.C032598`.

[17] Cartieri, A., "Experimental investigations on the Common Research Model at ONERA-S2MA," *AIAA Scitech 2020 Forum*, 2020, p. 0779. URL `https://doi.org/10.2514/6.2020-0779`.

[18] Vassberg, J., "A unified baseline grid about the Common Research Model wing/body for the Fifth AIAA CFD Drag Prediction Workshop," *29th AIAA Applied Aerodynamics Conference*, 2011, p. 3508. URL `https://doi.org/10.2514/6.2011-3508`.

[19] Hue, D., "DPW5: Structured grids from the MB point-matched family modified to match experimental wing twist in CGNS format," , 2013. `https://dpw.larc.nasa.gov/DPW5/contrib/HUE_CRM_twisted_grids_1` [Accessed: April 2023].

[20] "DPW5: Original (REV01) multi-block grids converted to hexes, prisms, and hybrid meshes," , 2012. `https://dpw.larc.nasa.gov/DPW5/unstructured_grids.REV01` [Accessed: April 2023].

[21] Hue, D., and Renaud, T., "Unstructured meshes and computations for aircraft performance prediction on the wing-body CRM configuration," Tech. Rep. RT 12/30245 ELSA/DAAA, ONERA, 2020.

[22] "5th International Workshop on High Order CFD Methods," , 2018. URL `https://how5.cenaero.be/`.

[23] Karman, S., "DPW6: Pointwise curved meshes," , 2017. `https://how5.cenaero.be/content/cr1-common-research-model` [Accessed: April 2023].

[24] Melber-Wilkending, S., "DPW7: NASA CRM SOLAR Grids for Case 1a," , 2022. `https://dpw.larc.nasa.gov/DPW7/DLR_Grids.REV00` [Accessed: April 2023].

[25] Jägersküpper, J., and Vollmer, D., "On highly scalable 2-level-parallel unstructured CFD," *8th European Congress on Computational Methods in Applied Sciences and Engineering, ECCOMAS Congress 2022*, 2022. URL `https://doi.org/10.23967/eccomas.2022.208`.

[26] Mohnke, J., and Wagner, M., “A Look at Performance and Scalability of the GPU Accelerated Sparse Linear System Solver Spliss,” *European Conference on Parallel Processing*, Springer, 2023, pp. 637–648.

[27] Schwöppe, A., and Diskin, B., “Accuracy of the Cell-Centered Grid Metric in the DLR TAU-Code,” *New Results in Numerical and Experimental Fluid Mechanics VIII: Contributions to the 17th STAB/DGLR Symposium Berlin, Germany 2010*, edited by A. Dillmann, G. Heller, H.-P. Kreplin, W. Nitsche, and I. Peltzer, Springer Berlin Heidelberg, Berlin, Heidelberg, 2013, pp. 429–437. URL `https://doi.org/10.1007/978-3-642-35680-3_51`.

[28] Langer, S., Schwöppe, A., and Leicht, T., “Comparison and Unification of Finite-Volume Discretization Strategies for the Unstructured Node-Centered and Cell-Centered Grid Metric in TAU and CODA,” *New Results in Numerical and Experimental Fluid Mechanics XIV*, edited by A. Dillmann, G. Heller, E. Krämer, C. Wagner, and J. Weiss, Springer Nature Switzerland, Cham, 2024, pp. 262–272.

[29] Barth, T., and Jespersen, D., “The design and application of upwind schemes on unstructured meshes,” *27th Aerospace sciences meeting*, 1989, p. 366. URL `https://doi.org/10.2514/6.1989-366`.

[30] Venkatakrishnan, V., “Convergence to steady state solutions of the Euler equations on unstructured grids with limiters,” *Journal of Computational Physics*, Vol. 118, No. 1, 1995, pp. 120–130. URL `https://doi.org/10.1006/jcph.1995.1084`.

[31] Blazek, J., *Computational Fluid Dynamics: Principles and Applications*, Elsevier Science Ltd., 2001.

[32] Bassi, F., and Rebay, S., “A high-order accurate discontinuous finite element method for the numerical solution of the compressible Navier–Stokes equations,” *Journal of Computational Physics*, Vol. 131, No. 2, 1997, pp. 267–279. URL `https://doi.org/10.1006/jcph.1996.5572`.

[33] Bassi, F., Crivellini, A., Rebay, S., and Savini, M., “Discontinuous Galerkin solution of the Reynolds-averaged Navier–Stokes and k–ω turbulence model equations,” *Computers & Fluids*, Vol. 34, No. 4-5, 2005, pp. 507–540. URL `https://doi.org/10.1016/j.compfluid.2003.08.004`.

[34] Basile, F., Chapelier, J.-B., Laraufie, R., and Frey, P., “Hybrid RANS/LES Simulations and Aeroacoustic Analysis of Jet Flows using an hp-Adaptive Discontinuous Galerkin Method,” *Flow, Turbulence and Combustion*, 2022, pp. 1–35. URL `https://doi.org/10.1007/s10494-022-00376-0`.

[35] Basile, F., Chapelier, J.-B., de la Llave Plata, M., Laraufie, R., and Frey, P., “Unstructured h-and hp-adaptive strategies for discontinuous Galerkin methods based on a posteriori error estimation for compressible flows,” *Computers & Fluids*, Vol. 233, 2022, p. 105245. URL `https://doi.org/10.1016/j.compfluid.2021.105245`.

[36] Cambier, L., Heib, S., and Plot, S., “The Onera elsA CFD software: input from research and feedback from industry,” *Mechanics & Industry*, Vol. 14, No. 3, 2013, pp. 159–174. URL `https://doi.org/10.1051/meca/2013056`.

[37] Jameson, A., Schmidt, W., and Turkel, E., “Numerical solution of the Euler equations by finite volume methods using Runge Kutta time stepping schemes,” *14th fluid and plasma dynamics conference*, 1981, p. 1259. URL `https://doi.org/10.2514/6.1981-1259`.

[38] Langer, S., Schwöppe, A., and Kroll, N., "The DLR Flow Solver TAU - Status and Recent Algorithmic Developments," *52nd Aerospace Sciences Meeting*, 2014, p. 0080. URL `https://doi.org/10.2514/6.2014-0080`.

[39] Dwight, R., "Efficiency Improvements of RANS-Based Analysis and Optimization using Implicit and Adjoint Methods on Unstructured Grids," Ph.D. thesis, Faculty of Engineering and Physical Sciences, University of Manchester, 2006.

[40] Spalart, P., and Allmaras, S., "A one-equation turbulence model for aerodynamic flows," *30th aerospace sciences meeting and exhibit*, 1992, p. 439. URL `https://doi.org/10.2514/6.1992-439`.

[41] Allmaras, S., Forrester, J., and Spalart, P., "Modications and Clarications for the Implementation of the Spalart-Allmaras Turbulence Model," *7th International Conference on Computational Fluid Dynamics*, 2012. URL `https://www.iccfd.org/iccfd7/assets/pdf/papers/ICCFD7-1902_paper.pdf`.

[42] Destarac, D., and Van Der Vooren, J., "Drag/thrust analysis of jet-propelled transonic transport aircraft; definition of physical drag components," *Aerospace Science and Technology*, Vol. 8, No. 6, 2004, pp. 545–556. URL `https://doi.org/10.1016/j.ast.2004.03.004`.

[43] Hue, D., and Esquieu, S., "Computational drag prediction of the DPW4 configuration using the far-field approach," *Journal of Aircraft*, Vol. 48, No. 5, 2011, pp. 1658–1670. URL `https://doi.org/10.2514/1.C031337`.

[44] Benoit, C., Péron, S., and Landier, S., "Cassiopee: a CFD pre-and post-processing tool," *Aerospace Science and Technology*, Vol. 45, 2015, pp. 272–283. URL `https://doi.org/10.1016/j.ast.2015.05.023`.

[45] Levy, D. W., Laflin, K. R., Tinoco, E. N., Vassberg, J. C., Mani, M., Rider, B., Rumsey, C. L., Wahls, R. A., Morrison, J. H., Brodersen, O. P., et al., "Summary of data from the fifth computational fluid dynamics drag prediction workshop," *Journal of Aircraft*, Vol. 51, No. 4, 2014, pp. 1194–1213. URL `https://doi.org/10.2514/1.C032389`.

[46] Keye, S., Togiti, V. K., and Brodersen, O. P., "DLR results of the sixth AIAA computational fluid dynamics drag prediction workshop," *35th AIAA Applied Aerodynamics Conference*, 2017, p. 4232. URL `https://doi.org/10.2514/6.2017-4232`.

[47] Glasby, R. S., and Erwin, J. T., "Introduction to COFFE: the next-generation HPCMP CREATETM-AV CFD solver," *54th AIAA aerospace sciences meeting*, 2016, p. 0567. URL `https://doi.org/10.2514/6.2016-0567`.

[48] Reza Ahrabi, B., and Mavriplis, D. J., "Scalable solution strategies for stabilized finite-element flow solvers on unstructured meshes," *55th AIAA Aerospace Sciences Meeting*, 2017, p. 0517. URL `https://doi.org/10.2514/6.2017-0517`.